

Effects of non-uniform rheology on the motion of bubbles in a yield-stress fluid

M. Zare¹, M. Daneshi² and I.A. Frigaard^{1,2,†}

¹Department of Mathematics, University of British Columbia, Vancouver, BC V6T 1Z2, Canada

²Department of Mechanical Engineering, University of British Columbia, Vancouver, BC V6T 1Z4, Canada

(Received 5 February 2021; revised 30 March 2021; accepted 6 April 2021)

Experimentally, when bubbles rise through yield-stress fluids they create a pathway that is preferentially followed by subsequent bubbles. The formation of such paths is not fully understood rheologically. Here, we instead study the effect of pathways, modelled as a pathway within which the yield stress is destroyed. We study how bubbles rise along such ‘damaged’ channels and how they may be trapped by a combination of capillary effects and the yield stress of the surrounding fluid. We then study the effects of these channels on distant bubbles. We show that the damaged channels attract bubbles that are mobile but lie at a distance well beyond the yielded envelope of the bubble. Angled channels also attract bubbles, that may either move along the channel or migrate outside. Experiments illustrate these behaviours, which are quantified in a series of two-dimensional computations. The study is motivated by interest in bubble release mechanisms in mined tailing ponds.

Key words: bubble dynamics

1. Introduction

Tailings ponds are used around the world in mining and other industrial processes. They incorporate engineered dam and dyke facilities used for storage of tailings materials, with the long-term objective of enabling water to separate from the tailings and eventual capping/land reclamation. In the case of mined oil sands, the tailings consist of coarse sands, fine clays, silt, water, residual and unrecovered bitumen, naphtha, naphthenic acids, petroleum hydrocarbons and other extraction bi-products. These are deposited in the ponds as they are produced. Coarse sands form beaches upon discharge and some sediment to the pond bottom. Above this forms a gradient ranging from mature fine tailings (MFT) to fluid fine tailings (FFT), topped with a clear water zone. Tailing ponds are thus mostly

† Email address for correspondence: frigaard@math.ubc.ca

stratified depthwise, with only slow lateral variations, and evolve over time scales of 1–10 years.

Our study is motivated by the bubble dynamics in oil-sand tailing ponds, as well as in other types of geo-materials. All oil-sand tailing ponds produce carbon dioxide (CO₂) (Small *et al.* 2015). In operations where naphtha has been used as the diluent, anaerobic bio-degradation of naphtha produces both methane (CH₄) and CO₂. Similar mechanisms in geological materials, such as shallow marine terrestrial sediments and in some flooded soils, also lead to the formation of CO₂ and CH₄ bubbles. These materials are not all transparent, but evidence of bubbles is found by sampling and acoustic measurements (Boudreau 2012). It has also been observed that bubbles can escape to the overlying water or the atmosphere (Leifer & Boles 2005; Walter *et al.* 2006). Gas emission is an evident environmental concern. There is also a range of fascinating fluid mechanical questions that arise.

Through the tailings deposition process and regular environmental changes in pressure and temperature (including freezing/thawing), it is clear that ponds undergo slow variations over large spatial (and temporal) scales. On a more local scale, bubble migration creates channel-like connecting conduits in the lower layer of the pond. Images collected from Base Mine Lake clearly show pockmarks on the interface of the water and FFT layer, providing evidence for associated chimneys below (Zhao *et al.* 2021). They have examined this phenomenon experimentally by injecting bubbles into a two-layer Newtonian-viscoplastic fluid system. They observed that the rising bubbles create a ‘damaged’ pathway through the lower layer, entrain some of the lower fluid into the water layer and that water subsequently flows down the pathway.

The FFT layer has been characterized rheologically as a thixotropic yield stress fluid (Derakhshandeh 2016). Thus, bubble rise (or trapping) is highly dependent on the yield stress and structure of the material in which bubbles are formed. Formation of ‘damaged’ pathways, with or without water intrusion, makes this layer rheologically non-uniform and challenges predictions that have been made based on uniform fluid properties. Transient bubble motion in a viscoplastic material with spatially varying rheology has not been studied before to our knowledge, and our aim here is explore whether damaged pathways can be modelled in this way. Although we have an industrial and environmental motivation, the study has a much broader relevance. Experimentally, any objects moving through any viscoplastic fluids will leave behind a ‘damaged’ trail. This phenomenon has been observed in a number of studies investigating the motion of bubble in viscoplastic fluids (Dubash & Frigaard 2007; Sikorski, Tabuteau & de Bruyn 2009; Lopez, Naccache & de Souza Mendes 2018; Zare & Frigaard 2018; Pourzahedi, Zare & Frigaard 2021). For example, in injecting a sequence of bubbles, subsequent ones follow the same trajectory as the first one and their size reduces and speed increases dramatically (Zare & Frigaard 2018), i.e. this is not a negligible effect. Similar effects are found in experiments with settling particles and flows around obstacles.

Perhaps the most relevant studies are those concerning the flow around bubbles in viscoplastic materials. A significant number of fluids used in our daily life (toothpaste, hair gel and peanut butter, tile adhesive, . . .), as well as working fluids in geophysical and industrial settings, (basaltic lava, cement slurries, drilling fluids, . . .), are categorized as viscoplastic fluids (Balmforth, Frigaard & Ovarlez 2014; Coussot 2017). The key feature of viscoplastic fluids is their yield stress. More precisely if such fluids are subjected to a stress more than their yield stress they deform and flow, otherwise they exhibit a solid-like behaviour. The simplest constitutive law used to describe the behaviour of these materials

is the Bingham fluid (Bingham 1922), which in tensorial form is given by

$$\hat{\tau} = \left[\hat{\mu}_p + \frac{\hat{\tau}_Y}{\hat{\gamma}} \right] \hat{\gamma} \iff \hat{\tau} > \hat{\tau}_Y, \quad (1.1)$$

$$\hat{\gamma} = 0 \iff \hat{\tau} \leq \hat{\tau}_Y. \quad (1.2)$$

Here, $\hat{\tau}$ and $\hat{\gamma}$ are the deviatoric stress and strain rate. The 2 model parameters are the plastic viscosity $\hat{\mu}_p$ and the yield stress $\hat{\tau}_Y$. The nonlinearity of the effective viscosity makes the prediction of the motion of bubbles in viscoplastic materials non-trivial. Discrimination between yielded and unyielded domains is *a priori* unknown, as are the yield surfaces delineating the yield domain.

A unique feature of bubbles in viscoplastic material is their entrapment. Bubbles may become entrapped when their buoyancy cannot overcome the resistance resulting from the yield stress of the material. The dependence of the critical bubble volume on the yield stress of the material has been showed in early studies such as Astarita & Apuzzo (1965). The authors performed a series of experiments with a range of non-Newtonian fluids and observed a sudden increase in the bubble velocity above a critical volume in viscoplastic fluids. Trapping is associated with the balance between yield stress and the buoyancy stress, captured in the dimensionless yield number Y . The conditions under which bubbles remain static have been formulated using variational principles by Dubash & Frigaard (2004), with crude estimates also made (Dubash & Frigaard 2007). The authors have found that the shape of bubble has significant effects on the bubble stopping conditions. Stein & Buggisch (2000) examined the stability of bubbles under external pressure oscillation theoretically and experimentally. They initially assume a spherical symmetry around a bubble, which is yielded due to the elasticity of the material, and solve for the flow in that region. Then they calculate the position of the yield surface from the perturbed velocity and stress fields, and finally the drag coefficient.

For computational studies, two techniques have been commonly used to resolve the nonlinearity of the constitutive equation: viscosity regularization and augmented Lagrangian techniques. Tsamopoulos and co-workers (Tsamopoulos *et al.* 2008) carried out an extensive computational study of axisymmetric steady bubble rise in a Bingham fluid. Their code was carefully validated for Newtonian fluids against both experimental and computational results. Although not a transient solution, their method iterates on the shape of the bubble using a mapping method until a steady solution is found. A regularization method was used in Tsamopoulos *et al.* (2008). Later, the authors compared their results to those calculated using an augmented Lagrangian method (Dimakopoulos, Pavlidis & Tsamopoulos 2013a), finding quite similar results and extending the study to Herschel–Bulkley fluids. Other authors have since computed the transient behaviour of axisymmetric bubbles in Bingham fluids (Tripathi *et al.* 2015; Karapetsas *et al.* 2019). Singh & Denn (2008) performed transient two-dimensional (2-D) computations for Stokes flows of Bingham fluids around bubbles. They explored entrainment and coalescence phenomena with multiple bubbles, the range of influence of adjacent bubbles and other effects of proximity. Here we also compute 2-D transient flows around bubbles. The choice of 2-D computations may appear strange for bubble motion. Due to the nonlinearity, fully 3-D transient computations are prohibitively expensive, even with regularized viscosity approaches. However, the phenomena we wish to study are asymmetric and the use of axisymmetric codes simply misses the phenomena of interest.

There are discrepancies between experimental and computational studies of bubble rise in viscoplastic fluids. First, there are deficiencies in constitutive laws such as the

frequently used Bingham and Herschel–Bulkley yield-stress models. These models have no elasticity and both build-up and breakdown of structure are assumed to be reversible and instantaneous. Secondly, these constitutive deficiencies manifest in observably different behaviours. For example, experimental results show that the initial bubbles injected into a column of viscoplastic fluid tend to ‘damage’ the fluid as the bubble rises. This ‘damage’ manifests as memory (subsequent bubbles are of different size but follow the same path as the first bubble) and as a reduced drag. Plausibly, this is an elastic effect, i.e. resulting from the internal stress history. The effects of history and preferential path on subsequent bubbles are themselves topics of considerable interest, studied in different contexts (Mougin, Magnin & Piau 2012; Lopez *et al.* 2018). Lopez *et al.* (2018) inserted a rigid rod into the fluid at an angle and manually removed it to create a damaged zone. They then let the fluid rest for 24 h before injecting bubbles. Their results show that bubbles deviate towards the damaged zone and rise along the path of the damaged zone. Both the preferential path experiments and those deliberately creating a damaged path provide significant evidence for how history effects may lead to formation of a non-uniform rheological medium and conduit structures in the lower strata of tailing ponds.

To avoid history effects, many researchers study only the passage of a single bubble through the fluid (typically Carbopol). For example, in Dubash & Frigaard (2007), the bubble column was emptied, the fluid sheared and the column refilled, i.e. between each bubble. In Sikorski *et al.* (2009) the authors report extensively mixing the fluids for a week before their experiments and at times during the experiments. In Lopez *et al.* (2018) and Wang *et al.* (2019) the fluid is mixed *in situ* following each bubble rise. Despite these precautions, there are still discrepancies with the computational results. In particular, experimental bubbles tend to form pointed tails as they rise, which has been attributed to either viscoelasticity or to the injection conditions. In Pourzahedi *et al.* (2021) this phenomenon has been studied using a complex layered structure, through which we are able to eliminate the effects of bubble injection but still find similar bubble shapes. It appears that newer visco-elasto-plastic rheological models may be able to represent this tail feature effectively (J. Tsamopoulos, private communication 2021).

In this study, we investigate the flow field around the bubbles rising in a medium with non-uniform rheology. As discussed above, the non-uniformity can be caused by motion of an object through a viscoplastic fluid, leaving behind a ‘damaged’ path. In tailing ponds, damaged paths are created by the rise of bubbles that are generated by anaerobic bio-degradation of naphtha. The rate of bubble generation varies due to many parameters, such as temperature, pressure and naphtha availability. Hence, the non-uniformity may arise on large length scales or time scales due to operational and/or seasonal variation. Here, we target more local variations such as may correspond to preferential pathways in large expanses of otherwise uniform yield-stress fluid. The notion that these pathways are somehow ‘damaged’ is modelled most simply by assuming that the pathways are Newtonian and of lower viscosity than the effective viscosity of the surrounding yield-stress fluid. Although one could experiment with different models for pathway generation (and/or water invasion of channels), there are many possible approaches and we postpone that complexity.

Here, we start with the simplest representative cases: the motion of a bubble rising in a yield-stress fluid enclosing a conduit of Newtonian fluid. We have investigated the transient shape and the trajectory of bubbles. We look at bubbles initiated within the conduit (e.g. as in a bubble invasion experiment) and also bubble placed off centre (e.g. as a study of proximity effects on bubbles moving or trapped in the FFT). The results are obtained using a combination of computational and experimental methods.

The paper starts by introducing the methodology. The flow equations and description of the numerical algorithms are given in § 2.1. A brief explanation of our experimental procedure is given in § 2.2. Our experiments are presented with the numerical results, to exemplify the different scenarios via proof-of-concept experiments. Benchmark results for the steady-state rise of single bubbles in a Bingham fluid, over a range of Archimedes and Bond numbers are presented in § 3 together with other benchmark results on the numerical algorithm. The main results of our study, focused on three specific scenarios, are presented in § 4 as follows. First, the motion of a bubble initially positioned in a narrow layer of Newtonian fluid surrounded by a yield-stress fluid is investigated in § 4.1. In § 4.2, the trajectory of a bubble placed in the vicinity of a layer of Newtonian fluid in a yield-stress fluid is studied. The rising trajectory of a bubble placed in an angled Newtonian layer crossing a yield-stress fluid is presented in § 4.3. The paper ends with a brief summary of results and conclusions; see § 5.

2. Methodology

Two methodologies are used in this study. First, we compute the motion of 2-D bubbles in a yield-stress fluid with varying rheology. The choice of 2-D computations contradicts the 3-D nature of the phenomena of interest. However, due to the nonlinear behaviour of the fluids, 3-D computations are prohibitively expensive. The 2-D computations allow the study of asymmetrical effects in the flow, that are key. The second method used is experimental.

2.1. Governing equations and computational method

Our main interest is in phenomena that are driven by rheological and buoyancy effects. Our bubble flows are initiated from rest and although the bubble motions may become inertial, the bubble-rise distances of interest are relatively small. Consequently, all fluids are considered incompressible in our study. The flow around a rising bubble is governed by the momentum and mass balances, which are made dimensionless. We scale all lengths with the equivalent radius, \hat{R}_b , of a circular bubble of the same area. We scale velocities with \hat{U} , obtained by balancing buoyancy and viscous forces, i.e. $\hat{U} = \hat{\rho}\hat{g}\hat{R}_b^2/\hat{\mu}_p$, where $\hat{\rho}$ is the density, \hat{g} is the gravitational acceleration (acting in direction \mathbf{e}_g), and $\hat{\mu}_p$ is the plastic viscosity of the surrounding viscoplastic fluid. Pressure and other stresses are scaled with $\hat{\rho}\hat{g}\hat{R}_b$. The scaled momentum and continuity equations are given by

$$\rho Ar[\mathbf{u}_t + \mathbf{u} \cdot \nabla \mathbf{u}] = -\nabla p + \nabla \cdot \boldsymbol{\tau} + \frac{k\mathbf{n}\delta_s}{Bo} + \rho \mathbf{e}_g, \quad (2.1)$$

$$\nabla \cdot \mathbf{u} = 0, \quad (2.2)$$

where \mathbf{u} , p , $\boldsymbol{\tau}$ denote the velocity, pressure and deviatoric stress, respectively.

The flow is governed principally by 3 dimensionless numbers. Two of these are the Archimedes number ($Ar = \hat{\rho}^2 \hat{R}_b^3 \hat{g} / \hat{\mu}_p^2$), and the Bond number, ($Bo = \hat{\rho} \hat{g} \hat{R}_b^2 / \hat{\sigma}_s$), where $\hat{\sigma}_s$ is the surface tension coefficient. A volumetric force formulation has been adopted for the surface tension, and this term appears on the right-hand side of the Navier–Stokes equations, where k is the mean curvature, \mathbf{n} the normal unit vector and δ_s is a surface Dirac δ -function that is non-zero only on the interface. Dimensionally, this term is $\hat{\mathbf{f}} = \hat{\sigma}_s k \mathbf{n} \delta_s$, where $\mathbf{n} \delta_s$ is approximated from ∇C , which is the gradient of volume fraction. In the numerical scheme, this term is evaluated using height functions (Popinet 2009).

The bubble is modelled using a volume of fluid (VoF) method. Equations (2.1) and (2.2) remain valid throughout the flow. In the liquid phase, the scaled density is $\rho = 1$ and in the bubble $\rho = \rho_b \ll 1$. The bubble is also assigned a small constant Newtonian viscosity $\hat{\mu}_b$. Thus, the constitutive law within the bubble is

$$\boldsymbol{\tau}(\mathbf{u}) = m_b \dot{\boldsymbol{\gamma}}(\mathbf{u}), \tag{2.3}$$

for $m_b = \hat{\mu}_b / \hat{\mu}_p \ll 1$, and where $\dot{\boldsymbol{\gamma}}(\mathbf{u})$ is the strain rate tensor

$$\dot{\boldsymbol{\gamma}}(\mathbf{u}) = \nabla \mathbf{u} + (\nabla \mathbf{u})^T. \tag{2.4}$$

The bubble density is fixed at $\rho_b = 0.001$. The bubble viscosity ratio m_b varies with the selected Ar , as we consider Ar to vary through changing the plastic viscosity. Nevertheless, for all m_b studied we have $m_b \ll 0.002$.

The liquid phase is a Bingham fluid modelled by

$$\boldsymbol{\tau}(\mathbf{u}) = \left[1 + Y \frac{1 - e^{-N|\dot{\boldsymbol{\gamma}}(\mathbf{u})|}}{|\dot{\boldsymbol{\gamma}}(\mathbf{u})|} \right] \dot{\boldsymbol{\gamma}}(\mathbf{u}), \tag{2.5}$$

where the yield number (Y) is defined as

$$Y = \frac{\hat{\tau}_Y}{\hat{R}_b \hat{\rho} \hat{g}}. \tag{2.6}$$

Here, $\hat{\tau}_Y$ denotes the yield stress of the Bingham fluid and Y represents the competition between yield and buoyancy stresses. Equation (2.5) is a commonly used smooth regularization of the exact Bingham constitutive equation proposed by Papanastasiou (1987). The regularization parameter $N \gg 1$ controls the closeness of approximation to the exact Bingham fluid model: $1/N$ represents a small (scaled) strain rate below which the fluid becomes very viscous, i.e. for $N|\dot{\boldsymbol{\gamma}}(\mathbf{u})| \ll 1$, we find at leading order that (2.5) becomes

$$\boldsymbol{\tau}(\mathbf{u}) \sim NY \dot{\boldsymbol{\gamma}}(\mathbf{u}). \tag{2.7}$$

In dimensional terms the strain rate and $1/N$ are scaled with $\hat{U}/\hat{R}_b = \hat{\rho} \hat{g} \hat{R}_b / \hat{\mu}_p$.

Later in our paper we investigate phenomenologically the effects on bubble motion of ‘damage’ to the gel, by considering included regions of purely Newtonian fluid, as in our experiments. Here, the two liquids are also modelled using the VoF formulation. Both are considered miscible as well as iso-dense ($\rho = 1$). Thus, there is no additional interfacial term required in (2.1). Although miscible, the experimental time scale and length scales are such that the Péclet number between liquids is extremely large and molecular diffusive effects can be neglected, i.e. the VoF model is physically appropriate. Where we have Newtonian liquid in our flows, this is modelled by

$$\boldsymbol{\tau}(\mathbf{u}) = m \dot{\boldsymbol{\gamma}}(\mathbf{u}), \tag{2.8}$$

where the viscosity ratio $m = \hat{\mu}_N / \hat{\mu}_p$, and $\hat{\mu}_N$ denotes the viscosity of the Newtonian fluid.

Our simulations are computed in a large rectangular domain (100×100). Boundary conditions for the simulation are no slip on the walls at both the sides and the top of the domain. At the bottom of the domain ($y = 0$) the pressure is set to zero as is the y -derivative of the normal velocity. The fluids are initially static. The initial bubble shape is circular and placed in the lower part of the flow domain, away from the boundaries.

Within the Bingham fluid significant strain rates are confined to the vicinity of the bubble. These yielded zones are estimated through a series of benchmark computations for different Y , Ar and Bo ; see § 3. The width of the domain is significantly larger than the yielded zone width. The height of the domain is tall enough to allow for transients of interest to be captured.

The VoF method is combined with a quadtree adaptive mesh refinement technique to accurately track the interfaces between the two or three phases. The local mesh refinement densifies the grid in regions of strong spatial variations of the velocity, fluid concentrations and the strain rate $|\dot{\gamma}(\mathbf{u})|$. The algorithm is implemented in the open source multi-phase flow solver Basilisk (based on the algorithms of the former Gerris), which is specifically suited to such applications (Popinet 2003, 2009; Fuster & Popinet 2018). The system of equations is resolved using a time-splitting projection method described in Popinet (2009). A physically motivated maximum timestep is imposed and further controlled via a Courant-Friedrichs-Lewy (CFL) constraint. The velocity advection term is estimated using the Bell–Colella–Glaz second-order upwind scheme at the intermediate timestep. The values of viscosity, density and pressure at the intermediate timestep are also used.

Basilisk uses the interpolation error between a field value at a grid point belonging to a grid level n and its interpolated value from a coarser grid level $n-1$ as a criterion to either coarsen or refine the grid locally, by merging 4 squares into a parent square or slicing a square into 4 sub-squares in two dimensions, respectively. The grid is refined or coarsened depending on whether this interpolation error is larger or smaller than 10^{-3} , 10^{-3} , 10^{-9} for velocity, concentrations and strain rate, respectively. The domain is initially divided into 128×128 cells. Each of these may subdivided according to the refinement, to a maximum of 9 quadtree levels. Spurious currents are also minimized by using a height function method to estimate the interface curvature. Basilisk has been widely validated against analytical, numerical and experimental interfacial flows. Basilisk is frequently used for Newtonian bubble flow calculations, including flows significantly more challenging than those studied here (Balla *et al.* 2019; Berny *et al.* 2020; Zhang *et al.* 2020).

In benchmarking our code we have experimented with various values of N . For extreme N the rapidly changing effective viscosity results in convergence problems, as is often reported. As we increase $N > 10^4$ we find only minor changes in the terminal velocity of the computed bubbles; see figure 1, computed for $Ar = 50$, $Bo = 5$. To explore convergence with respect to N , we regard the solution at $N = 5 \times 10^5$ as the converged numerical solution and compute the relative error of the L^2 norm of the solution

$$d\|U\|_{L^2} = \frac{\|U_{N=5 \times 10^5} - U_N\|_{L^2}}{\|U_{N=5 \times 10^5}\|_{L^2}}, \quad (2.9)$$

as N is increased from $N = 10^2$, see the inset of figure 1. As the quadtree mesh refinement procedure is automated, it can be slightly different for different N . Thus, to find the relative error, we have mapped the solution obtained with different values of N , onto a fixed mesh with constant spatial spacing. For $N \geq 3 \times 10^4$ we see that relative error of the velocity field does not change appreciably: the L^2 norm of the relative error is $\sim 10^{-3}$. This constant discrepancy is attributed to the interpolation error caused by mapping of data. For the remainder of the computations of the paper we use $N = 5 \times 10^4$.

2.2. Experimental set-up and material

A series of experiments have also been performed to visualize the effects of a thin channel of Newtonian liquid on a bubble rising in a column of a viscoplastic fluid.

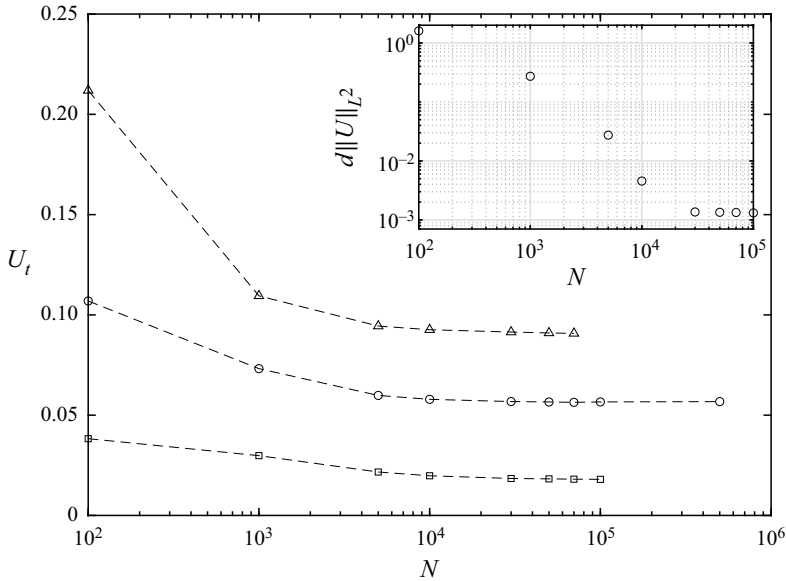


Figure 1. The variation of the magnitude of the bubble-rise terminal velocity calculated with different values of N for $(\circ) Ar = 50, Bo = 5, (\square) Ar = 500, Bo = 5, (\triangle) Ar = 1, Bo = 50$. The L^2 norm of deviation of the velocity solutions for $Ar = 50, Bo = 5$ with a range of N from the solution with $N = 5(10^5)$ is plotted in the inset.

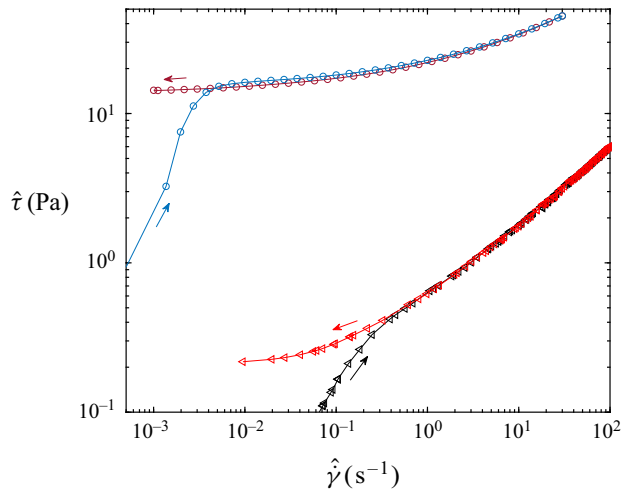


Figure 2. Flow curves for the Carbowol 0.06% and 0.15% solutions are measured by a stress controlled ramp-up and ramp-down test. The triangles and circles denote the data obtained for the Carbowol 0.06% and 0.15%, respectively. The fluid properties are found by the Herschel–Bulkley fit as $\hat{\tau}_Y = 14.61 \text{ Pa}, n = 0.39$ and $\hat{k} = 8.8 \text{ Pa s}^n$ for the 0.15% solution and $\hat{\tau}_Y = 0.2 \text{ Pa}, n = 0.57$ and $\hat{k} = 0.39 \text{ Pa s}^n$ for the 0.06% solution.

Our experiments are conducted in an acrylic column with height 49.5 cm and width 9.7 cm (square cross-section). In order to introduce the Newtonian fluid, two narrow tubes with inner diameters of 9.7 and 19 mm and outer diameters of 12 and 25.5 mm, respectively were used. We also used a drinking straw with diameter of ~ 5 mm and negligible wall thickness. In each experiment, the tube of desired size is first placed inside the acrylic box

in the desired position/angle and is sealed against the bottom wall of the box. The box is filled with the viscoplastic fluid. Then, water was poured into the tube, dyed to aid in visualization. Finally, the tube has been pulled up slowly from the column. The fluids have similar densities, the viscoplastic fluid is held static by its yield stress and the configuration is observed to remain stable and static during this operation. We then injected bubbles into the column using a syringe pump at a rate of 5 ml min^{-1} to start the experiment. The size of bubbles varies in the range 8–18 mm. The apparatus is shown later in the experimental results and described in more detail in Pourzahedi *et al.* (2021).

The motion and shape of bubbles were recorded using a DSLR camera. The results are presented in spatio-temporal images in § 4. These are collated (using the difference between images) to form spatio-temporal figures, shown later. The yield-stress fluid used in our experiments is a 0.15 % wt Carbopol solution, which is widely used as a model viscoplastic fluid for experiments. The flow curve of the material, i.e. the stress–strain rate relation, is measured by a shear stress controlled ramp-up and ramp-down test and is illustrated in figure 2. The material exhibits elastic behaviour below the yield point and shear-thinning behaviour above the yield stress. Thixotropic and viscoelastic effects are minimal at the concentrations that we use, which are fairly typical for bubble propagation experiments (Dubash & Frigaard 2007; Lopez *et al.* 2018; Pourzahedi *et al.* 2021). Preparation details are as in Zare & Frigaard (2018).

3. Bubble rise in a Bingham fluid

We first consider the rise of a single 2-D bubble in a Bingham fluid, to establish the reliability of the computational method and provide benchmark results for later researchers. With the exception of Singh & Denn (2008), who treated non-inertial bubble flows, we have not found results for 2-D bubble motions. Here, we fix $Y = 0.1$, which is below the critical values Y_c at which a 2-D bubble is trapped by the yield stress (Chaparian *et al.* 2020), and we release the bubbles from a circular initial shape. One reason for considering $Y < Y_c$ is that the main phenomena of interest for our study are transient. Secondly, the use of a regularization method (2.5) is not ideal for studying the limit $Y \rightarrow Y_c^-$. Comparisons between solutions computed using regularization and those using a (slower but more accurate) augmented Lagrangian algorithm have been made by Dimakopoulos, Pavlidis & Tsamopoulos (2013b) for axisymmetric bubble computations.

Our bubbles are initially static and released with a circular shape. They rise and deform, eventually reaching a steady terminal velocity (U_t) and shape. We study a range of Ar and Bo , presenting the results at the final steady-state condition in figure 3. In these figures we plot the bubble shape, the streamlines and the contour of the yield criterion. The latter is defined as the level set of $|\dot{\gamma}(\mathbf{u})|$, for which $|\tau(|\dot{\gamma}(\mathbf{u})|)| = Y$. The shaded colour maps present $\log |\dot{\gamma}(\mathbf{u})|$. As expected, our results confirm that the flow around the bubble is limited to within a yielded region of fluid. The size and shape of the yield surfaces as well as the bubble deformation depend on Ar and Bo . The steady-state shape and the computed terminal velocity U_t and other numerical values are tabulated in table 1.

For larger Ar , the role of inertia is more significant and the yield surfaces are not fore–aft symmetric. As Bo increases, the surface tension is not large enough to retain the shape of the bubble as circular. At small Ar , the bubble elongates along its axis of gravity and takes an elliptical shape (see figure 3c), while at larger Ar , the bubble is deformed to a more oblate shape under the effect of inertia. Our computational results at low Ar resemble the shapes of the non-inertial bubbles computed by Singh & Denn (2008). For the larger Ar and Bo , a region of low strain rate appears at its rear. The bubble is eventually flattened at its rear and a quasi-triangular unyielded wake region forms at its rear (figures 3(g) and

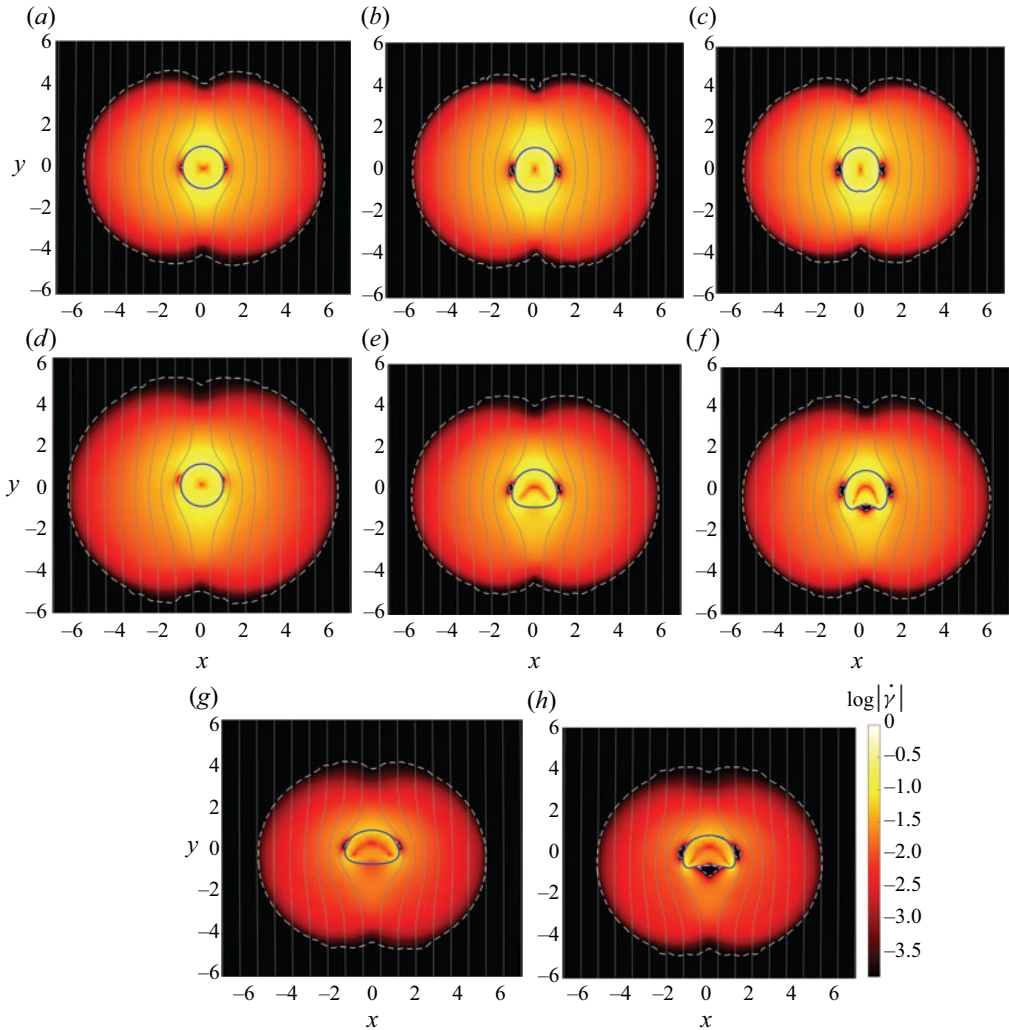


Figure 3. Map of Steady flow field and bubble shapes in a Bingham fluid ($Y = 0.1$) as a function of the Bond and Archimedes numbers; (a) $Ar = 1, Bo = 0.01$, (b) $Ar = 1, Bo = 5$, (c) $Ar = 1, Bo = 50$, (d) $Ar = 50, Bo = 0.01$, (e) $Ar = 50, Bo = 5$, (f) $Ar = 50, Bo = 50$, (g) $Ar = 500, Bo = 5$, (h) $Ar = 500, Bo = 50$. The blue line represents the bubble interface. The contours represent $\log |\dot{\gamma}|$, while the streamlines and the yield surfaces are plotted with grey lines and white dashed lines, respectively. The parameters used for numerical simulations and quantified results regarding the shape and terminal velocity of the bubble are given in table 1.

3(h)), the size of which increases with Ar . A further interesting point is that the strain rate vanishes close to the bubble equator, which in almost all cases leads to the formation of unyielded ‘ears’ attached to the sides of bubbles. Similar features are observed in Singh & Denn (2008) and Chaparian *et al.* (2020). Qualitatively, the range of shapes and the parametric changes are similar to those in previous computations of axisymmetric bubbles (Tsamopoulos *et al.* 2008; Dimakopoulos *et al.* 2013b; Tripathi & Sahu 2018).

Our computations retain left–right symmetry and evolve smoothly towards the steady shape, suggesting stability. This process also appears to be stable with respect to the initial conditions. In figure 4 we show the evolution of a bubble for $Ar = 1, Bo = 5, Y = 0.1$, in which an initial inverted teardrop shape is assumed. As observed the bubble evolves to

Ar	Bo	m_b	U_t	AR
1	0.01	$4.9(10^{-5})$	0.071	1
1	5	$4.9(10^{-5})$	0.086	1.09
1	50	$4.9(10^{-5})$	0.092 (0.112*)	1.15
50	0.01	$3.5(10^{-4})$	0.079,(0.0757*)	1
50	5	$3.5(10^{-4})$	0.056,(0.059*)	0.84
50	50	$3.5(10^{-4})$	0.059	0.9
500	0.01	10^{-3}	0.049	1
500	5	10^{-3}	0.018	0.62
500	50	10^{-3}	0.017	0.63

Table 1. The viscosity ratio (m_b), terminal velocity (U_t) and aspect ratio of bubble ($AR = \text{height/width}$), for cases shown in figure 3, are listed here. Terminal velocities with (*) are obtained based on the augmented Lagrangian method (described in Chaparian *et al.* 2020) and are reported here for the sake of comparison with our numerical results. Note that in all of these simulations, the yield number is $Y = 0.1$, the regularization parameter is fixed at $N = 5(10^4)$ and the density ratio is $\rho_b = 0.001$.

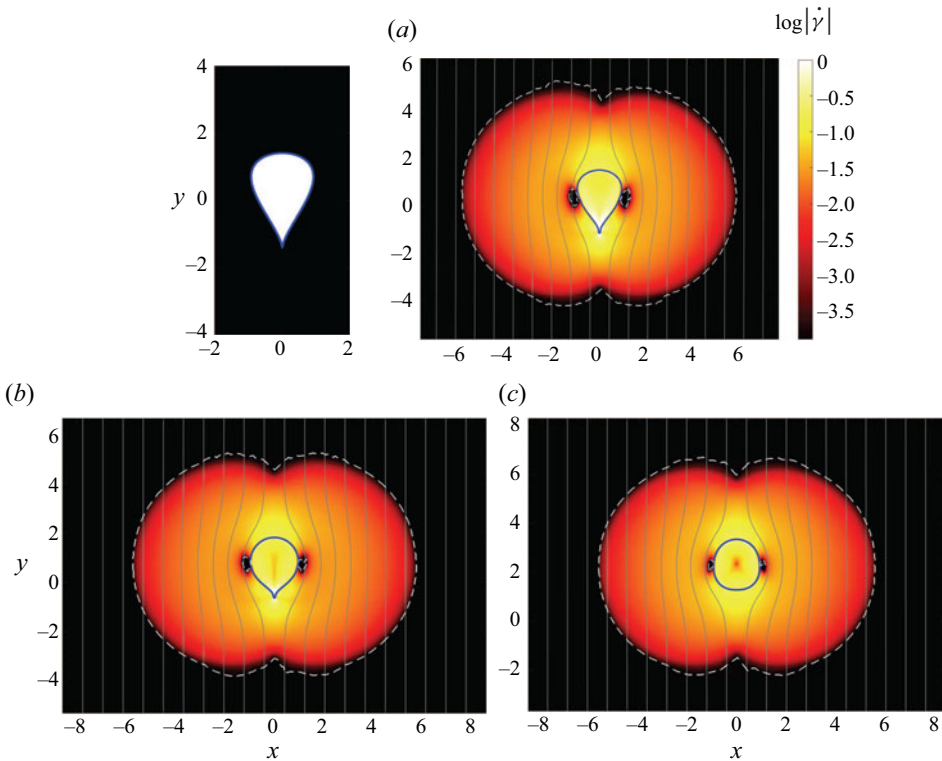


Figure 4. Evolution of shape of a bubble and flow field around it as it rises in a Bingham fluid. The bubble initially has an inverse teardrop shape. The results are obtained for $Ar = 1, Bo = 5, Y = 0.1$, at (a) $t = 1$, (b) $t = 5$, (c) $t = 60$. The contours and lines are defined the same as those plotted in figure 3.

the same steady shape of an initially circular bubble; see figure 4(b). Recent experiments using a system of layered fluids have also found that the terminal shape and velocity in a yield-stress fluid layer are not strongly dependent on the initial bubble configuration (Pourzahedi *et al.* 2021).

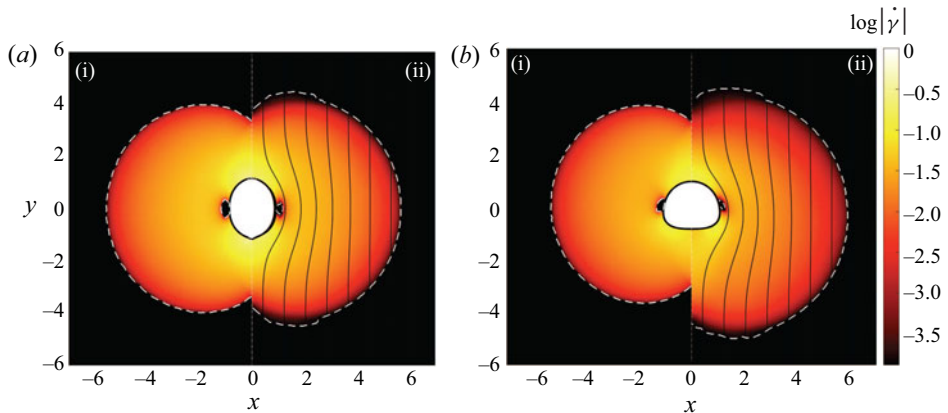


Figure 5. Comparison between results obtained from a steady-state augmented Lagrangian method (Chaparian *et al.* 2020) (i), and those obtained from our numerical simulations (ii), for (a) $Ar = 1, Bo = 50, Y = 0.1$, and (b) $Ar = 50, Bo = 5, Y = 0.1$. The contours and lines are defined the same as those plotted in figure 3.

Lastly, we have benchmarked our numerical algorithm by comparing our results for steady-state rising bubbles with those obtained from a steady-state augmented Lagrangian based algorithm. The augmented Lagrangian method provides more accurate computation of the yield surface, but has only been implemented for steady flows. Briefly, we extract the terminal bubble shape from our transient computations and use this interface for a steady-state computation. Thus essentially, the comparison is between resolution of the regularized Bingham–Navier–Stokes system (in a converged steady flow) and a non-regularized Bingham–Navier–Stokes system, for the same interface geometry. The comparison is made directly in figure 5 for two different cases, showing both results in both (a) and (b) of the same figure. The discrepancies are mainly in the position of the yield surface away from the bubble surface and the differences are quite similar to those for axisymmetric bubbles computed in Dimakopoulos *et al.* (2013b). In addition, the terminal velocity obtained based on these two models differs by less than five per cent.

4. Results

We explore three different set-ups in which bubble rise in a viscoplastic fluid is affected by the presence of a thin channel of Newtonian fluid. This is motivated by the scenarios discussed in § 1 and by different observations. First, gas invasion or bubble-rise experiments through yield-stress fluids, such as in Zare & Frigaard (2018) and Pourzahedi *et al.* (2021), characteristically affects the rheology of the fluid in the vicinity of where the first bubbles pass. Typically, successive bubbles follow an identical vertical pathway where the fluid has been sheared by the previous bubbles. Although undoubtedly the result of elasticity or thixotropy, a simple model for the history effect of the prior bubble passage is to assume that the yield stress of the fluid has been ‘damaged’.

A second more direct analogy comes from the development of entrained water channels within a gel layer, as observed by Zhao *et al.* (2019), when bubbles exit a gelled layer into an overlaying water layer. Although more direct, the precise mechanisms underlying this phenomenon are not yet understood. Thus, we use the Newtonian layer as a proxy for a ‘damaged’ yield-stress fluid layer.

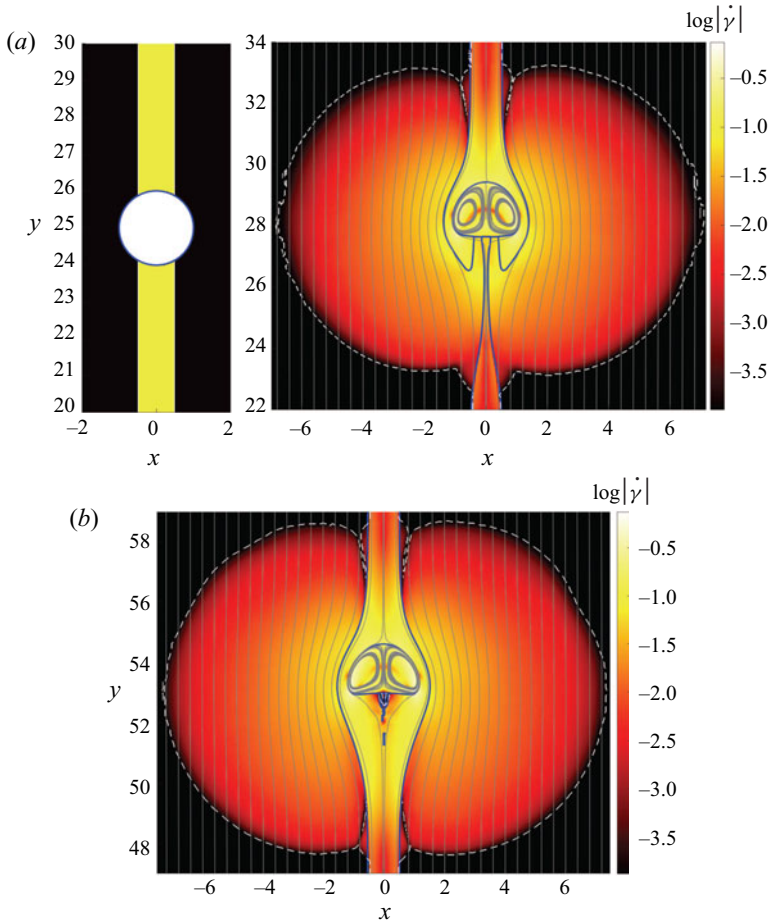


Figure 6. Flow around a bubble rising in a layer of Newtonian fluid, with thickness of $L = 1$, surrounded by a Bingham fluid. The results were obtained for $Ar = 50$, $Bo = 5$, $Y = 0.1$ at $t = 0, 50, 350$, from (a) to (b). Terminal velocity and aspect ratio are $U_t = 0.08$ and $AR = 0.7$, respectively. The contours and lines are defined the same as those plotted in figure 3.

4.1. Bubble rise in an embedded Newtonian layer

To explore the effect of a ‘damaged’ yield stress on bubble motion we consider a thin vertical layer of Newtonian fluid surrounded by a yield-stress fluid. The bubble is initially circular and positioned at the centre of the Newtonian layer, with all fluids at rest. The viscosity ratio is fixed at $m = 1$ so that we investigate the elimination of yield-stress and shear-thinning effects within a local channel.

We present results for $Ar = 50$, $Bo = 5$ and $Y = 0.1$ in figure 6. The thickness L of the Newtonian channel is the initial bubble radius, $L = 1$. The flow contours, yield surfaces and the streamlines for $Ar = 50$, $Bo = 5$, $Y = 0.1$ at $t = 50$ and $t = 350$ are illustrated. The flow field is plotted in terms of contours of $\log|\dot{\gamma}|$, with the lower bound for the colour scale equal to the critical value of shear rate at which the yield stress is attained for the scaled Bingham–Papanastasiou model. Streamlines are also shown as solid lines with grey colour and the yield surface with a broken line.

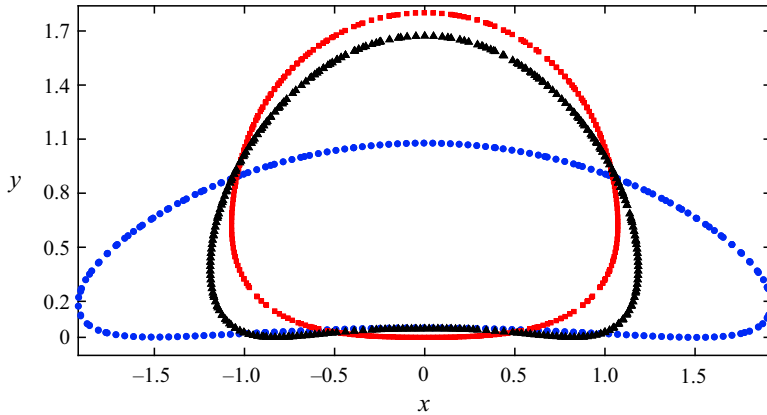


Figure 7. Steady-state shape of a bubble at $Ar = 50$, $Bo = 5$ and in a Newtonian fluid, (\circ , blue), a Bingham fluid $Y = 0.1$ (see figure 3e), (\square , red) and a Newtonian layer surrounded by a Bingham fluid $Y = 0.1$ (see figure 6), (\blacktriangle).

The bubble deforms from its initially circular shape into a chestnut shape. As the bubble rises, a film of viscous fluid drains around the bubble and, over time, the bubble rises entirely within the Newtonian layer. The viscous Newtonian layer apparently provides a lower dissipation path than the surrounding yield-stress fluid for the bubble. The terminal velocity of the bubble, $U_t = 0.08$, is higher than that of the bubble in a uniform Bingham fluid, ($U_t = 0.06$) and lower than that of the bubble in a uniform Newtonian fluid $U_t = 0.126$.

Interestingly, on comparing the size of yielded region with that obtained for a bubble in a uniform Bingham fluid at the same parameters (figure 3e), we see that a larger area of the Bingham fluid has been yielded here. This appears to be counter-intuitive from the perspective of lubrication, i.e. as the less viscous Newtonian layer might be thought of as localizing the strain rates and hence confining the stress: apparently this does not happen. The larger stress field is presumably the result of the higher velocity of the bubble and consequently higher shear rate at the interface of the two liquids, compared with the air–viscoplastic fluid interface.

The other effect observed is on the bubble shape. Figure 7 shows shapes of the steady bubble rise in a uniform Newtonian, uniform Bingham fluid and in the Newtonian layer, which have aspect ratios $AR = 0.28, 0.84, 0.7$, respectively. The bubble deforms more in the Newtonian layer than in the uniform Bingham fluid, but the far field Bingham fluid still acts to constrain the deformation. We see that the shape is very different from the bubble in a uniform Newtonian fluid.

In studying the steady bubble rise in § 3, we found that the buoyancy force is not enough to yield the fluid surrounding the bubble at $Y = 0.25$ for $Ar = 50$, $Bo = 5$, i.e. the bubble is trapped. Large $Bo > 1$ suggests that surface tension is not important and we may compare $Y = 0.25$ with the exact critical yield number for a circular bubble with no surface tension ($Y_c = 0.171$), as computed in Chaparian & Tammsola (2020). Here, however, we find that if the bubble is surrounded partly by the Newtonian fluid channel it may escape and move up. Figure 8 shows the flow field around the bubble for $Ar = 50$, $Bo = 5$, $Y = 0.25$.

Interestingly, during the initial time steps, the bubble deforms and elongates in order to fit into the Newtonian layer. The shape of bubble in figure 8 is quite different from figure 6,

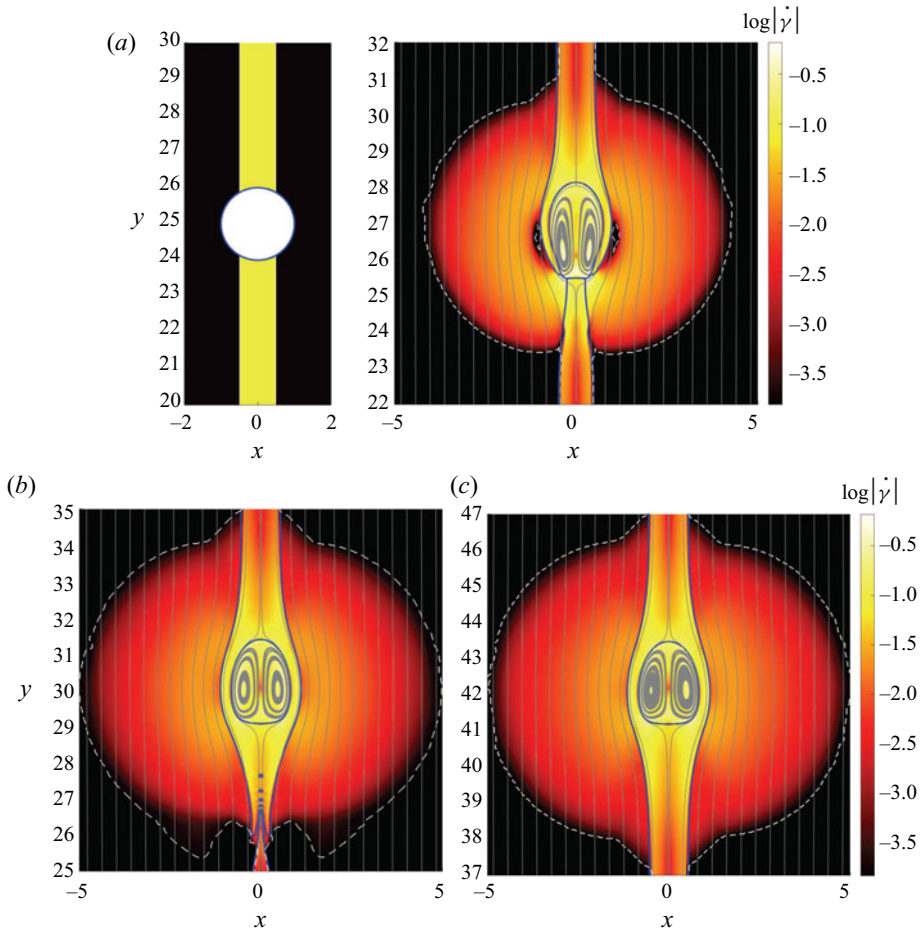


Figure 8. Flow around a bubble rising in a layer of a Newtonian fluid, with thickness of $L = 1$, surrounded by a Bingham fluid. The results were obtained for $Ar = 50$, $Bo = 5$, $Y = 0.25$ at $t = 0, 125, 200, 450$, from (a) to (c). Terminal velocity and aspect ratio of the bubble at the steady-state condition are $U_t = 0.05$ and $AR = 1.346$, respectively. The contours and lines are defined the same as those plotted in figure 3.

although the buoyancy and surface tensions are the same. By increasing Y , the bubble gets more elongated within the Newtonian layer and its aspect ratio increases. This is effectively due to the higher yield stress of the surrounding fluid constraining the deformation of the Newtonian channel. Consequently, we find a smaller yielded zone around the viscous layer. It is expected that by increasing $Y \rightarrow \infty$, the interface between the viscous and yield-stress fluids effectively becomes rigid. In this case the bubble must deform by initially shrinking and elongating so that it may move upwards in the Newtonian channel.

For a bubble rising in a capillary tube/channel, capillary blockage can occur when surface tension effects dominate. Here, due to the modest Bo , the bubble is able to change shape and migrate. However, by reducing the width L of the embedded channel from $L = 1$ progressively down to $L = 0.5$ it becomes progressively difficult for the buoyancy to overcome capillary effects, the terminal velocity reduces and we find that, for a layer width $L = 0.5$, the bubble does not rise, at least within the accuracy of our numerical scheme. The terminal velocities calculated, together with the terminal bubble shape, are plotted against L in figure 9.

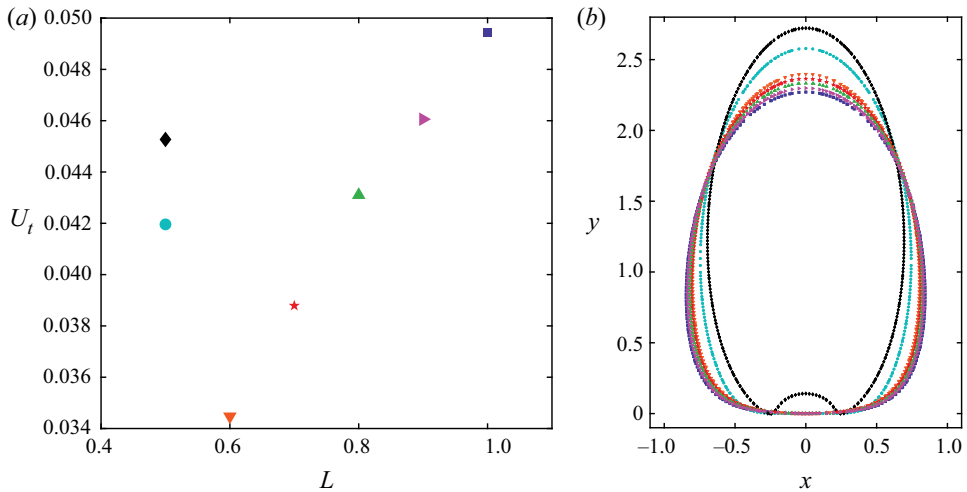


Figure 9. The variation of terminal velocity (a) and shape of bubble (b) rising in a Newtonian layer, with thickness of $L = 0.6, 0.7, 0.8, 0.9, 1$ for $Bo = 5$ and thickness of $L = 0.5$ for (\blacklozenge) $Bo = 50$ and (\bullet , cyan) $Bo = 10$, surrounded by a Bingham fluid. The results are obtained for $Ar = 50, Y = 0.25$.

In order to alleviate the capillary blockage at $L = 0.5$, we increase Bo (at fixed Ar and Y). As Y is fixed, this corresponds to a reduced surface tension. The bubble becomes more elongated along the Newtonian layer and the terminal velocity drops. A qualitative comparison between the stress fields obtained for these two cases suggests that the size of the yielded region decreases by increasing Bo . The higher terminal velocity and longer bubble in $Bo = 50$ results in a lower drag coefficient in comparison with that of $Bo = 10$. The recirculation zone behind the bubble makes an indentation at the lower side of bubble for $Bo = 50$.

4.2. Effects of an offset Newtonian layer

The second scenario that we consider is the effect of the Newtonian layer on bubbles that are nearby. In the industrial context, does the presence of the Newtonian channel affect the stability or movement of distant bubbles? We have investigated this scenario computationally for $Ar = 50, Bo = 5, Y = 0.1$ and again in a Newtonian layer of width $L = 1$. The bubble is initially positioned in the yield-stress fluid at a centre-to-centre distance of, $\Lambda = 5$. As observed in figure 3(e), the width of the yielded envelope around a single bubble in a uniform yield-stress fluid (for $Ar = 50, Bo = 5, Y = 0.1$) extends to $x \approx \pm 5$. Therefore, we expect that the bubble will ‘feel’ the Newtonian layer at its periphery.

The flow field and streamlines are shown in figure 10 at various times. The bubble initially deforms to a shape close to that of figure 3(e), but migrates laterally towards the Newtonian layer as it rises. Evidently the bubble senses the Newtonian layer via the stress field. The images show the approach and encapsulation of the bubble within the Newtonian layer. During the approach the Newtonian layer is deformed/squeezed. The fluid to the right of the channel is initially unaffected but yields as the bubble approaches. Finally the bubble rises vertically in the Newtonian layer as in figure 6, where $\Lambda = 0$.

A related question to the effect of the Newtonian layer is the effect of other bubbles on both stability and motion. This has been studied by Singh & Denn (2008), who show that, for sufficiently large spacing, two bubbles of a size that would individually be stable do not

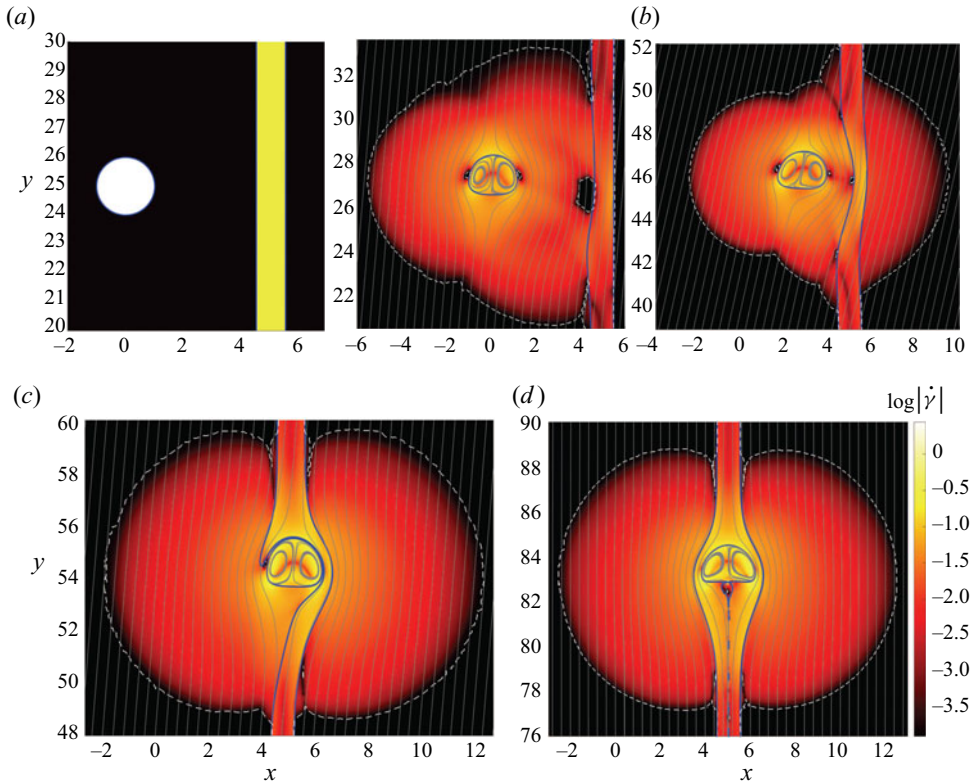


Figure 10. Flow around a rising bubble initially positioned in the yield stress fluid at a centre-to-centre distance of, $\Lambda = 5$, to a Newtonian layer. The results were obtained for $Ar = 50, Bo = 5, Y = 0.1$ at $t = 0, 50, 400, 550, 900$, from (a) to (d). Terminal velocity and aspect ratio of the bubble at the steady-state condition are $U_t = 0.08$ and $AR = 0.7$, respectively. The contours and lines are defined the same as those plotted in figure 3.

feel each other and remain trapped. Similar effects are found for trapped buoyant particles. Therefore, we question whether by extending Λ we reach a critical distance beyond which there is no influence of the Newtonian layer on the bubble motion.

We have computed the bubble motion for Newtonian layers placed at $\Lambda = 5, 7.5, 10, 12.5, 15$. We show the trajectory of the bubble centre in figure 11. It is expected that the bubble rises without deviating toward the Newtonian layer for $\Lambda > 5$, and this does happen for $\Lambda = 12.5, 15$. However, the results show that the bubble moves significantly towards the Newtonian channel at $\Lambda = 7.5$, and there is a very marginal effect at $\Lambda = 10$. Precise determination of a critical offset distance is difficult with the Bingham–Papanastasiou regularization, since the low shear rate flows are modelled as very viscous Newtonian flows, for which the stress decays very slowly with distance and the Newtonian channel must always induce a slight asymmetry in the ‘unyielded’ flow field around the bubble.

4.2.1. Illustrative experiments

We have performed a series of illustrative experiments with the methodology described in § 2.2. The purpose of the first series of experiments is to visualize the motion of a bubble injected into a column of Carbopol in which a vertical channel of reduced viscosity has

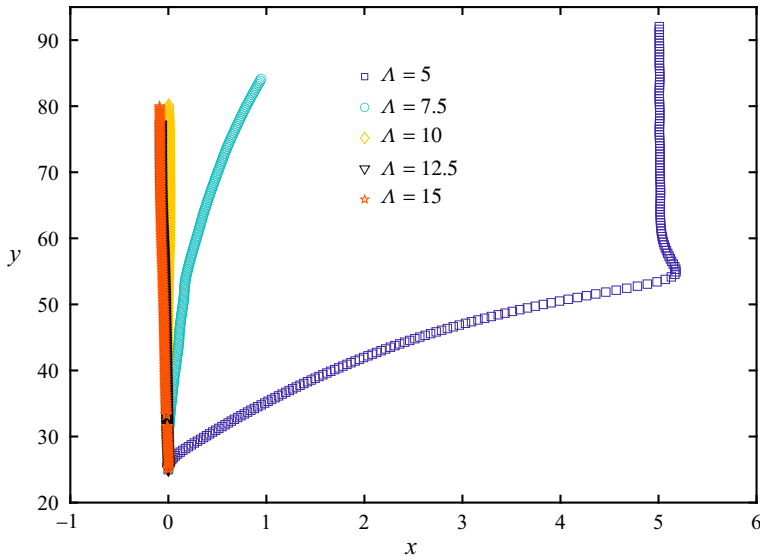


Figure 11. Trajectories of a bubble rising through a Bingham fluid which encompasses a thin vertical layer of a Newtonian fluid. The bubble is initially positioned at a distance of $\Lambda = 5, 7.5, 10, 12.5$ from the viscous layer. The dimensionless parameters are fixed at $Ar = 50, Bo = 5, Y = 0.1$.

been placed. The channel is either water or a lower concentration of Carbopol. Three experiments have been performed for this case and the results are shown in [figure 12](#).

In the first experiment, a narrow water tube (with a diameter of ~ 12 mm) is inserted within the column of 0.15 %-Carbopol and near the right wall of the tank. The bubble starts to rise in a vertical path without ‘feeling’ the water channel. We speculate that the yielded envelope around the bubble does not extend to the viscous channel, hence the bubble path is unaffected by the water channel. Indeed strangely we observe that the bubble path becomes slightly deviated toward the left side of the column; see [figure 12\(a\)](#). The Carbopol column is filled slowly using a funnel and, in all the experiments, its neck has been positioned on the left side of the column. This may produce a mild history effect from residual stresses of the filling process.

In the second test, we have placed a wider water tube (outer diameter 25.5 mm) on the right side of the column and have injected a significantly larger bubble than in the first experiment. We observe that bubble starts immediately to drift to the right side and enters the less viscous green fluid; see [figure 12\(b\)](#). A plausible explanation is that the yielded region is now larger and overlaps with the Newtonian channel. The resulting stress field affects the symmetry of the flow and the bubble drifts toward the water tube. We note the significant change in bubble shape on entering the water channel.

We have repeated the second experiment by placing a lower Carbopol concentration, 0.06 %, instead of water in the column of Carbopol 0.15 %. The spatio-temporal plot of the injected bubble motion is shown in [figure 12\(c\)](#). Again, the bubble moves into the less viscous channel. We note that the bubble is smaller than in [figure 12\(b\)](#) but released a similar lateral distance away (Λ in our computations). It is noticeable that the bubble enters the less viscous channel lower down than in [figure 12\(b\)](#). The smaller bubble does have smaller vertical velocity component, which might allow more time for the lateral propagation. We note that this scenario is of interest in the context of a large expanse of

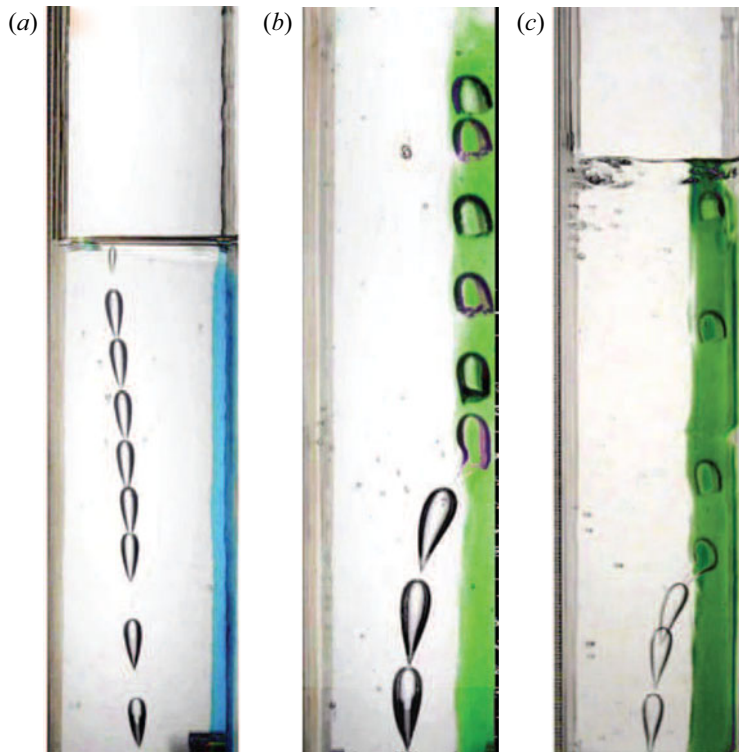


Figure 12. Spatio-temporal images of bubble motion in a fluid column consisting of Carbopol 0.15 % and a (a) 12 mm tube of water (dye blue); (b) 25.5 mm tube of water (dye green); (c) 25.5 mm tube of Carbopol 0.06 % (dye green). The results are obtained from experiments.

gelled fluid (e.g. a tailing pond) in which local rheology variations are quite natural, e.g. due to aging, different deposits and different settling history.

The main discrepancy between the experimental and computational results shown, apart from dimensionality, is in the shape of the bubble rising in Carbopol. The bubble develops a pointed shape at its lower end in Carbopol which markedly contradicts behaviour observed in the computational results. The inverted teardrop shape is likely due to the elasticity of the Carbopol, which is not present in the Bingham model that has been used in this study. The tail is not always present, e.g. it has been shown that bubbles do not develop a tail in yield-stress fluids at high Ar (Lopez *et al.* 2018; Pourzahedi *et al.* 2021). In this context, we note that the bubble in Carbopol 0.06 % looks similar to the bubble in the water tube and loses its tail, see figures 12(b) and 12(c). A slightly different feature of experiments vs computations is that the surface tension of yield stress fluids is not always easily measured and is not readily variable, i.e. we do not typically study wide ranges of Bo independent from other parameters.

We have further investigated the shape of bubbles in a viscous channel surrounded by a yield-stress fluid. Based on our computational results, we expect that the bubble becomes elongated in a narrow viscous layer; see figure 9. To explore this we have positioned a narrow water tube (outer diameter 5 mm) near to the injection point, inside our column of Carbopol of concentration 0.15 %; see figure 13(a). The spatio-temporal images of the injected bubble as it rises through the column are shown in figure 13(b). As observed, the bubble immediately after detachment deviates toward the water channel. It becomes

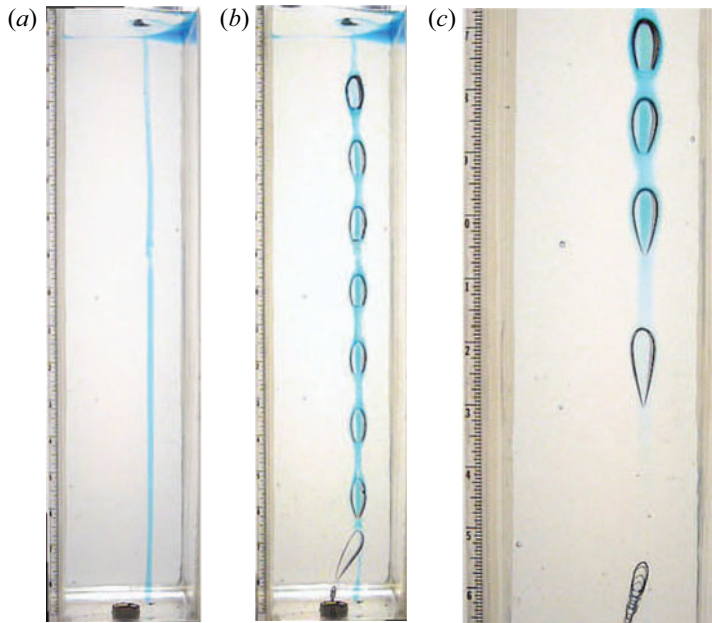


Figure 13. Experimental results obtained for a bubble rising inside a 5 mm tube of water (dyed blue) enclosed by Carbopol 0.15 %. The layout of the fluid column is shown in (a). The spatio-temporal images of the motion of the first and a subsequent bubble are shown in (b) and (c), respectively.

encapsulated in the Newtonian channel, the shape elongates and loses its tail. The shape near the top of the column is qualitatively similar to the bubbles in figure 9: prolate with a flat lower side. The volume of bubble in this experiment is $2065 \pm 110 \text{ mm}^3$ and its rise velocity in the Newtonian tube is $544.8 \pm 27 \text{ mm s}^{-1}$. This velocity is almost two times larger than the terminal velocity of a bubble with the same size rising in a large expanse of water, following the relation of Davies & Taylor (1950). Probably, the confinement to the tube reduces the drag on the bubble, i.e. due to having a smaller frontal area.

As successive bubbles are injected, they also orient towards the position of the water conduit. As observed by Zhao *et al.* (2021), each bubble pushes water up to the free surface. As a result, the lower part of the water conduit is depleted and contains only sheared Carbopol. Bubbles follow the same ‘damaged’ or low resistance path. However, now the bubble shape does not change at the lower depths (angular tail) until it begins to enter the water column from below, after which the blunted prolate shape is again attained; see figure 13(c).

4.3. Angled layers

We now consider the effects of angled layers. Apart from the possibility of water entrainment, other formation mechanisms are plausible. First, as we have seen above, bubbles will move laterally towards a Newtonian channel in their migration. Each such migration leaves an angled pathway that will be remembered in the gel, and potentially influence adjacent bubbles. Thus, over time in the setting of a large expanse of gelled fluid, we may envision networks of angled ‘damaged’ pathways leading towards the same vertical channel through the gel. Secondly, again in the context of a large expanse of gelled

fluid, we might expect external factors such as freezing/melting, additional deposition of tailings, etc. to induce stresses/strains in the static gel at many different alignments.

An example of a computation for $Ar = 50$, $Bo = 5$, $Y = 0.25$ is shown in [figure 14](#). Here, $L = 0.95$ and the layer has been angled at $\theta = 72.5^\circ$ (from horizontal). As discussed in the previous section, at this Y the bubble cannot rise in the pure yield-stress fluid, but it does rise along a vertical Newtonian layer by adjusting its shape slightly. Here, we see that in the angled layer the bubble also rises, but evidently an asymmetric velocity field is generated. The bubble moves closer to the upper side of the layer, as might be expected. The Newtonian fluid that is displaced around the bubble thus moves predominantly around the lower side of the bubble. This has the interesting effect of a larger yielded region in the viscoplastic fluid on the lower side of the Newtonian layer.

It is evident that there is a competition between buoyancy and the yield stress in keeping the bubble within the Newtonian layer. The trajectory of bubbles for a range of Y values are plotted in [figure 15](#) for $Ar = 50$, $Bo = 5$ and at the same angle. At $Y = 0.25$ and $Y = 0.2$, the buoyancy is not big enough to push the bubble vertically outside the Newtonian channel; instead, it rises along the inclined channel where there is less resistance. By decreasing the yield number to $Y = 0.1$, buoyancy is able to move the bubble trajectory partly above the Newtonian layer. Interestingly, the bubble still propagates parallel to the Newtonian layer!

Decreasing the surface tension (increasing Bo), affects the shape change but the bubble still propagates within the Newtonian layer at $Y = 0.2, 0.25$; see [figure 15](#). In all of these cases, the Newtonian viscosity is the same as the plastic viscosity of the viscoplastic fluid, $m = 1$. By increasing m , we increase the resistance of the Newtonian layer and the bubble rises outside of the angled layer (for $Y = 0.1$). In [figure 15](#) we see that the Newtonian layer still exerts a considerable effect on the trajectory. Curiously, the bubble trajectory deviates linearly from that of the channel over the range computed. Presumably, this linear deviation is local and once sufficiently distant from the Newtonian layer the rise trajectory will become vertical.

Whereas, at $Y = 0.25$, in the absence of a Newtonian layer the bubble would be trapped in the viscoplastic, the same is not true at $Y = 0.1$. The bubble trajectory for $Ar = 50$, $Bo = 5$, $Y = 0.1$ in [figure 15](#) is thus non-trivial in moving partially outside the Newtonian layer. We explore this delicate balance more in [figure 16](#), where we consider the effects of different angled Newtonian layers on the motion.

The results show that, for $\theta \geq 60^\circ$, the bubble rises in the Newtonian layer, albeit partly extending outside. For smaller θ , the contribution of buoyancy component, perpendicular to the Newtonian layer, becomes more significant and moves the bubble out of the Newtonian layer. However, since the Newtonian layer still affects the stress field, the flow around the bubble is asymmetric and the bubble still deviates from the vertical direction.

We illustrate similar behaviour experimentally. In this experiment, a tube of blue coloured water with outer diameter of 12 mm is placed in our column of Carbopol 0.15 %, at an angle $\theta \approx 74^\circ$; [figure 17\(a\)](#). [Figure 17\(b\)](#) shows the passage of the first bubble. Interestingly, the bubble rises up and ‘feels’ the Newtonian channel, changes its path and initially moves to the right. As it enters the water channel, it re-routes and follows the angled path. As with the computations, the bubble is oriented to the upper side of the tube, due to buoyancy. In [figure 17\(c\)](#) we show the spatio-temporal images of a subsequent bubble.

Whereas [figure 15](#) explores the influence of inclined layers on mobile bubbles (i.e. $Y = 0.1 < Y_c$), such as might be created by prior bubble motion, lower in a tailing pond other mechanisms might be present. For example, temperature, atmospheric pressure

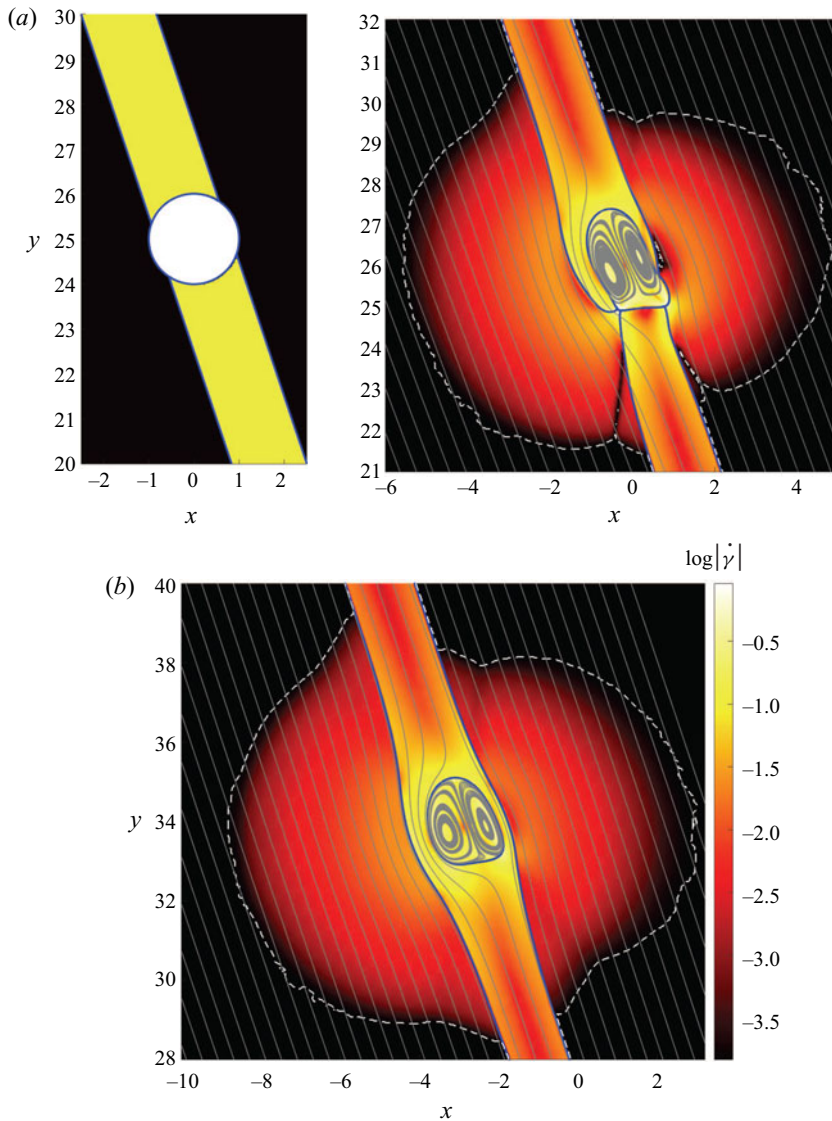


Figure 14. The flow and motion of a rising bubble in a viscous layer crossing a yield-stress fluid at $\theta = 72.5^\circ$. The results were obtained for $Ar = 50$, $Bo = 5$, $Y = 0.25$ at $t = 0, 45, 200$, from (a) to (b). The terminal speed of the bubble is $U_t = 0.055$. The contours and lines are defined the same as those plotted in figure 3.

or geomechanical stresses may induce faults/crevices within the FFT/MFT channels, or close to the interface with coarse sand, into which less viscous liquids may be squeezed. Thus, channels with slowly varying near horizontal inclinations may interconnect laterally. In figure 18 we show migration of bubbles laterally along such channels, computed for $Ar = 50$, $Bo = 5$, $Y = 0.25$ with a Newtonian layer angled at $\theta = 10$ and 20° . The larger Y confines the bubble to within the channel. Conceptually, such channel networks provide a means for smaller bubbles generated deep in the sediment to migrate and accumulate in a way that may eventually yield the surrounding fluid.

Viscoplastic flow with reaction

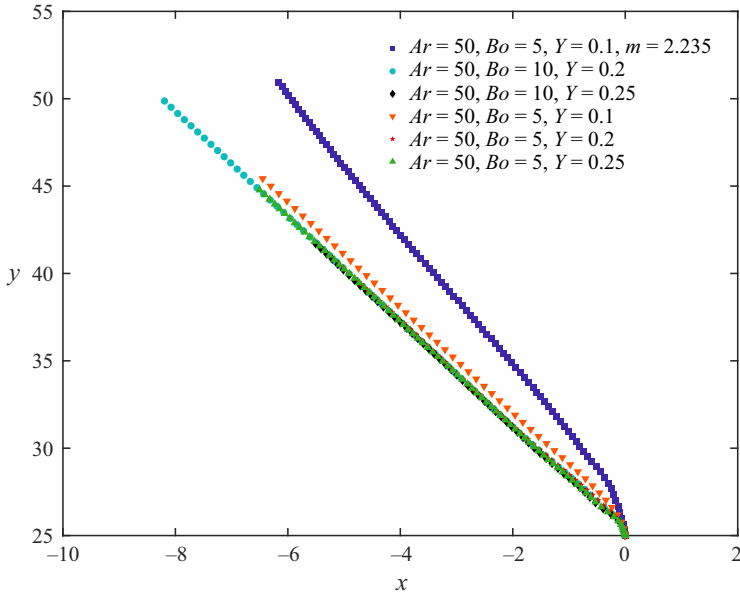


Figure 15. Trajectory of bubbles placed inside an angled layer of viscous fluid ($\theta = 72.5^\circ$) which is crossing the domain of a yield-stress fluid. The same computational scenario as explained in figure 14 was repeated here for different values of Bo and Y , as indicated.

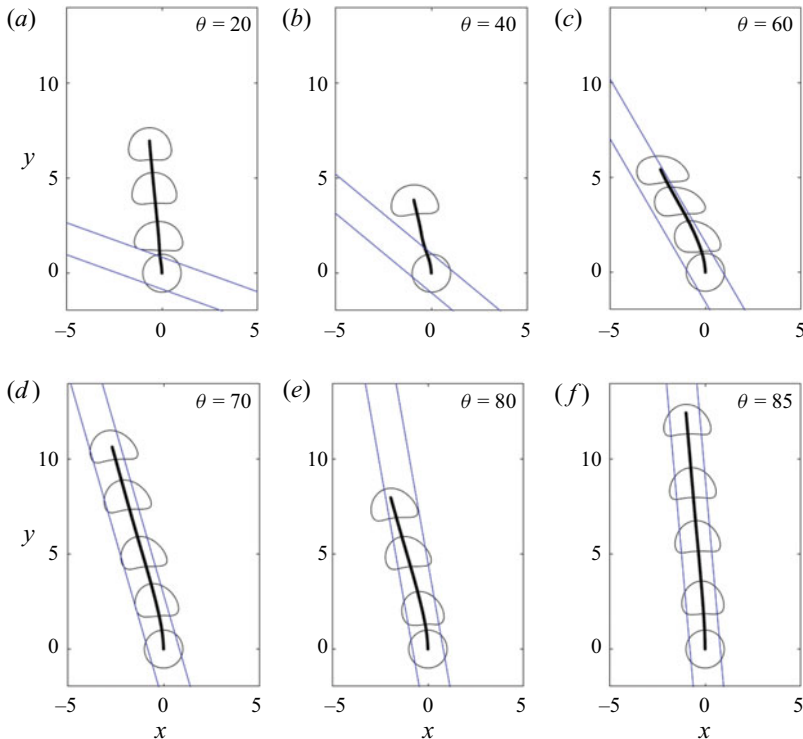


Figure 16. Spatio-temporal images of bubble rise in a tilted viscous layer crossing a yield-stress fluid. The variation of shape and trajectory of bubble with the angle of viscous layer (from horizontal) is shown here. The dimensionless flow parameters are fixed at $Ar = 50, Bo = 5, Y = 0.1$.

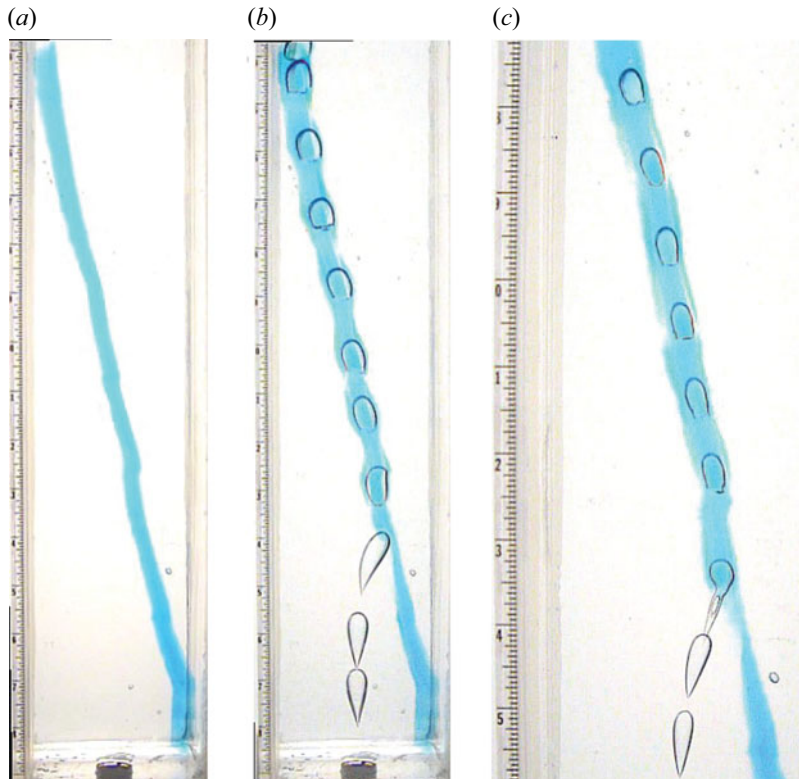


Figure 17. Experimental results obtained for a bubble rising in a yield-stress fluid that encompasses a tilted Newtonian channel. (a) The layout of the fluid column: a tube of blue dyed water (with outer diameter of 12 mm) is placed in Carbopol 0.15 %, at an angle of $\theta = 73.6^\circ$; (b,c) spatio-temporal images of the first bubble and a subsequent bubble rising through domain.

5. Summary

When successive bubbles migrate through a yield-stress fluid they preferentially follow the pathway of previous bubbles. Conceptually at least, the stresses induced by the preceding bubbles result in rheological changes within the fluid (whether via elasticity or thixotropy), such that the resistance of the fluid is reduced. These ‘damaged’ pathways are believed to be very relevant to the mechanisms by which gas bubbles can be released from oil-sand tailing ponds and other geological materials, such as shallow marine terrestrial sediments and some flooded soils.

Here, we have ignored the damage mechanism and modelled the preferential pathway by considering a Newtonian fluid conduit embedded within a viscoplastic main phase. Bubbles released centrally within the channel migrate upwards along the Newtonian channel. The Newtonian fluid flows down and around the bubble as it rises, deforming the surrounding viscoplastic fluid. The terminal bubble shapes are different than in either a pure Newtonian or pure viscoplastic fluid column. For increased yield stress the outer viscoplastic deforms less. The bubble may still propagate at yield-stress values for which it would be trapped in a pure viscoplastic fluid column. As the width of the Newtonian channel is decreased, the bubbles elongate. We find a critical width below which capillary blockage occurs, i.e. there is a second trapping mechanism.

Viscoplastic flow with reaction

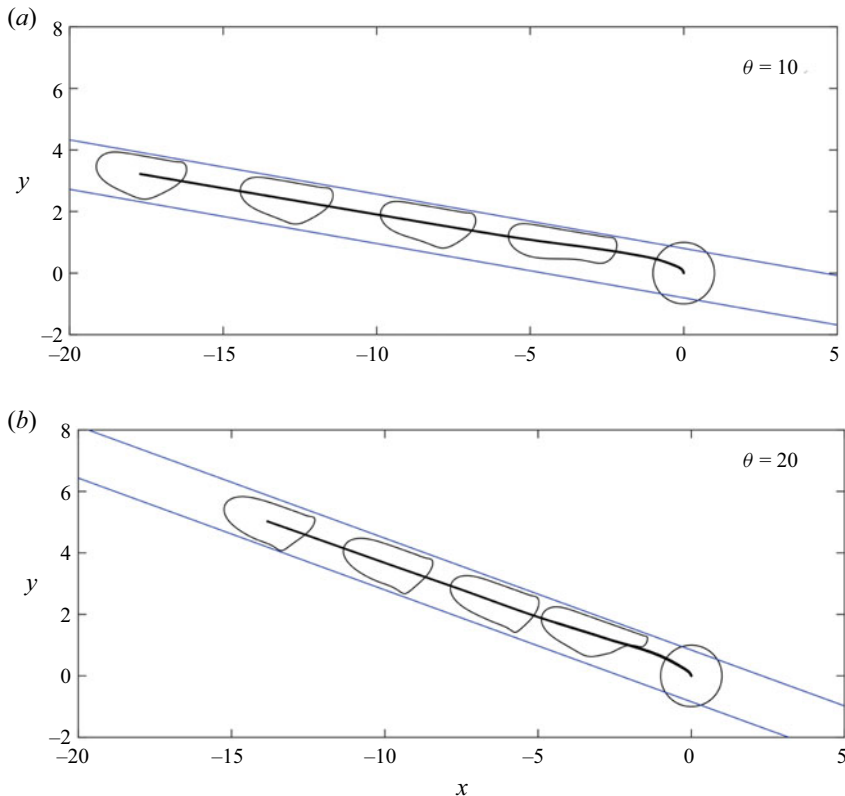


Figure 18. Spatio-temporal images of bubble rise in a tilted viscous layer crossing a yield-stress fluid. The dimensionless flow parameters are fixed at $Ar = 50$, $Bo = 5$, $Y = 0.25$.

Next, we explored the effects of damaged pathways on bubbles that are relatively close but positioned fully within the viscoplastic fluid. Bubbles moving alone in a viscoplastic fluid cause it to yield only within a finite envelope. We find that the influence of the stress field extends significantly further than this yielded envelope. Bubbles feel the Newtonian channel and migrate towards it. In the context of a broad region of dispersed similar bubbles in a tailing pond, this conjures the image of a network of pathways converging into nearby chimneys extending deep into the pond. This localization is both worrying, from the perspective that bubbles migrate/release easier, and promotes optimism from the perspective of controlling emissions. If the objective is to purge the pond of gas, a converging network is ideal. If the objective is to retain gas in the pond, disrupting/blocking chimneys or localized remixing are methods worth exploring.

In the last section of results we explored the effects of path inclination on preferential migration. The main observation is that, even for strongly inclined pathways, the influence is strong. While the pathways due to prior bubbles and attraction of nearby bubbles are close to vertical, we can imagine that larger scale pond gradients, e.g. due to tailing deposit operations, freezing/thawing, pond depth variations, etc. may all result in stress defects and hence preferential pathways oriented closer to horizontal. We have not yet fully explored the effects of such pathways, but results such as [figure 18](#) are enticing.

Methodologically, our computations have used a VoF implementation within the Basilisk adaptive framework. The bubble surface is tracked effectively and many other

authors have used this code for a range of bubble flows. Although there are other ways to track the interface, we feel this aspect is perfectly adequate for the flows considered. We have developed benchmark results for single bubbles and explored convergence with respect to the parameter N . Whether the regularization approach is adequate for all the flows one could consider is a different question. For example, in studying the effects of channel proximity on adjacent bubbles, the low shear rates deliver a very viscous fluid for which the stress decays slowly. Computations using the augmented Lagrangian method do deliver yielded regions outside of which there is no flow and would be better suited to giving definitive answers to some of the questions studied, albeit at additional computational cost.

The experiments illustrate clearly that the phenomena we study do actually occur, motivating further study by either method. Longer-term future directions include attempting to model the initial preferential path formation using more complete rheological models.

Funding. This research was made possible by collaborative research funding from NSERC and COSIA/IOSI (project numbers CRDPJ 537806-18 and IOSI Project 2018-10). Experimental infrastructure was partly funded by the Canada Foundation for Innovation and the BC Knowledge Development Fund, grant number CFI JELF 36069. This funding is gratefully acknowledged. This computational research was also enabled by infrastructure provided from Compute Canada/Calcul Canada (www.computecanada.ca).

Declaration of interests. The authors report no conflict of interest.

Author ORCID.

 I.A. Frigaard <https://orcid.org/0000-0002-0970-240X>.

REFERENCES

- ASTARITA, G. & APUZZO, G. 1965 Motion of gas bubbles in non-Newtonian liquids. *AIChE J.* **11** (5), 815–820.
- BALLA, M., TRIPATHI, M.K., SAHU, K.C., KARAPETSAS, G. & MATAR, O.K. 2019 Non-isothermal bubble rise dynamics in a self-rewetting fluid: three-dimensional effects. *J. Fluid Mech.* **858**, 689–713.
- BALMFORTH, N.J., FRIGAARD, I.A. & OVARLEZ, G. 2014 Yielding to stress: recent developments in viscoplastic fluid mechanics. *Annu. Rev. Fluid Mech.* **46**, 121–146.
- BERNY, A., DEIKE, L., SÉON, T. & POPINET, S. 2020 Role of all jet drops in mass transfer from bursting bubbles. *Phys. Rev. Fluids* **5** (3), 033605.
- BINGHAM, E.C. 1922 *Fluidity and Plasticity*, vol. 2. McGraw-Hill.
- BOUDREAU, B.P. 2012 The physics of bubbles in surficial, soft, cohesive sediments. *Mar. Petrol. Geol.* **38** (1), 1–18.
- CHAPARIAN, E., IZBASSAROV, D., DE VITA, F., BRANDT, L. & TAMMISOLA, O. 2020 Yield-stress fluids in porous media: a comparison of viscoplastic and elastoviscoplastic flows. *Meccanica* **55** (2), 331–342.
- CHAPARIAN, E. & TAMMISOLA, O. 2020 Complex sliding flows of yield-stress fluids. [arXiv:2004.02950](https://arxiv.org/abs/2004.02950).
- COUSSOT, P. 2017 Bingham's heritage. *Rheol. Acta* **56** (3), 163–176.
- DAVIES, R.M. & TAYLOR, G.I. 1950 The mechanics of large bubbles rising through extended liquids and through liquids in tubes. *Proc. R. Soc. Lond. A* **200** (1062), 375–390.
- DERAKSHANDEH, B. 2016 Kaolinite suspension as a model fluid for fluid dynamics studies of fluid fine tailings. *Rheol. Acta* **55** (9), 749–758.
- DIMAKOPOULOS, Y., PAVLIDIS, M. & TSAMOPOULOS, J. 2013a Steady bubble rise in Herschel–Bulkley fluids and comparison of predictions via the augmented Lagrangian method with those via the Papanastasiou model. *J. Non-Newtonian Fluid Mech.* **200**, 34–51.
- DIMAKOPOULOS, Y., PAVLIDIS, M. & TSAMOPOULOS, J. 2013b Steady bubble rise in Herschel–Bulkley fluids and comparison of predictions via the augmented Lagrangian method with those via the Papanastasiou model. *J. Non-Newtonian Fluid Mech.* **200**, 34–51.
- DUBASH, N. & FRIGAARD, I.A. 2004 Conditions for static bubbles in viscoplastic fluids. *Phys. Fluids* **16** (12), 4319–4330.
- DUBASH, N. & FRIGAARD, I.A. 2007 Propagation and stopping of air bubbles in Carbopol solutions. *J. Non-Newtonian Fluid Mech.* **142** (1–3), 123–134.

- FUSTER, D. & POPINET, S. 2018 An all-mach method for the simulation of bubble dynamics problems in the presence of surface tension. *J. Comput. Phys.* **374**, 752–768.
- KARAPETSAS, G., PHOTEINOS, D., DIMAKOPOULOS, Y. & TSAMOPOULOS, J. 2019 Dynamics and motion of a gas bubble in a viscoplastic medium under acoustic excitation. *J. Fluid Mech.* **865**, 381–413.
- LEIFER, I. & BOLES, J. 2005 Measurement of marine hydrocarbon seep flow through fractured rock and unconsolidated sediment. *Mar. Petrol. Geol.* **22** (4), 551–568.
- LOPEZ, W.F., NACCACHE, M.F. & DE SOUZA MENDES, P.R. 2018 Rising bubbles in yield stress materials. *J. Rheol.* **62** (1), 209–219.
- MOUGIN, N., MAGNIN, A. & PIAU, J.M. 2012 The significant influence of internal stresses on the dynamics of bubbles in a yield stress fluid. *J. Non-Newtonian Fluid Mech.* **171**, 42–55.
- PAPANASTASIOU, T.C. 1987 Flows of materials with yield. *J. Rheol.* **31** (5), 385–404.
- POPINET, S. 2003 Gerris: a tree-based adaptive solver for the incompressible euler equations in complex geometries. *J. Comput. Phys.* **190** (2), 572–600.
- POPINET, S. 2009 An accurate adaptive solver for surface-tension-driven interfacial flows. *J. Comput. Phys.* **228** (16), 5838–5866.
- POURZAHEDI, A., ZARE, M. & FRIGAARD, I.A. 2021 Constraining the origin of fore-aft asymmetrical shape of bubbles rising in yield stress fluids. *J. Non-Newtonian Fluid Mech.* (accepted for publication).
- SIKORSKI, D., TABUTEAU, H. & DE BRUYN, J.R. 2009 Motion and shape of bubbles rising through a yield-stress fluid. *J. Non-Newtonian Fluid Mech.* **159** (1–3), 10–16.
- SINGH, J.P. & DENN, M.M. 2008 Interacting two-dimensional bubbles and droplets in a yield-stress fluid. *Phys. Fluids* **20** (4), 040901.
- SMALL, C.C., CHO, S., HASHISHO, Z. & ULRICH, A.C. 2015 Emissions from oil sands tailings ponds: review of tailings pond parameters and emission estimates. *J. Petrol. Sci. Engng* **127**, 490–501.
- STEIN, S. & BUGGISH, H. 2000 Rise of pulsating bubbles in fluids with a yield stress. *Z. Angew. Math. Mech.* **80** (11–12), 827–834.
- TRIPATHI, M.K. & SAHU, K.C. 2018 Motion of an air bubble under the action of thermocapillary and buoyancy forces. *Comput. Fluids* **177**, 58–68.
- TRIPATHI, M.K., SAHU, K.C., KARAPETSAS, G. & MATAR, O.K. 2015 Bubble rise dynamics in a viscoplastic material. *J. Non-Newtonian Fluid Mech.* **222**, 217–226.
- TSAMOPOULOS, J., DIMAKOPOULOS, Y., CHATZIDAI, N., KARAPETSAS, G. & PAVLIDIS, M. 2008 Steady bubble rise and deformation in Newtonian and viscoplastic fluids and conditions for bubble entrapment. *J. Fluid Mech.* **601**, 123–164.
- WALTER, K.M., ZIMOV, S.A., CHANTON, J.P., VERBYLA, D. & CHAPIN, F.S. 2006 Methane bubbling from Siberian thaw lakes as a positive feedback to climate warming. *Nature* **443** (7107), 71–75.
- WANG, Z., LOU, W., SUN, B., PAN, S., ZHAO, X. & LIU, H. 2019 A model for predicting bubble velocity in yield stress fluid at low Reynolds number. *Chem. Engng Sci.* **201**, 325–338.
- ZARE, M. & FRIGAARD, I.A. 2018 Onset of miscible and immiscible fluids' invasion into a viscoplastic fluid. *Phys. Fluids* **30**, 063101.
- ZHANG, Y., DABIRI, S., CHEN, K. & YOU, Y. 2020 An initially spherical bubble rising near a vertical wall. *Intl J. Heat Fluid Flow* **85**, 108649.
- ZHAO, K., TEDFORD, E., ZARE, M., FRIGAARD, I. & LAWRENCE, G. 2019 Laboratory experiments on air bubbles rising through Carbopol capped with water. In *APS Division of Fluid Dynamics Meeting Abstracts* (ed. J. Cloern), p. A24.007. Wiley.
- ZHAO, K., TEDFORD, E., ZARE, M. & LAWRENCE, G. 2021 Impact of atmospheric pressure variation on methane ebullition and turbidity in an oil sands pit lake. [arXiv:2105.06383](https://arxiv.org/abs/2105.06383).